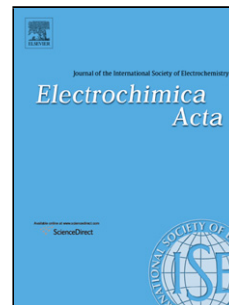Accepted Manuscript

Title: Graphene-like carbon sheet/Fe$_3$O$_4$ nanocomposites derived from soda papermaking black liquor for high performance lithium ion batteries

Authors: Xinli Yi, Wen He, Xudong Zhang, Yuanzheng Yue, Guihua Yang, Zhaoyang Wang, Maojuan Zhou, Lianzhou Wang

Please cite this article as: Xinli Yi, Wen He, Xudong Zhang, Yuanzheng Yue, Guihua Yang, Zhaoyang Wang, Maojuan Zhou, Lianzhou Wang, Graphene-like carbon sheet/Fe3O4 nanocomposites derived from soda papermaking black liquor for high performance lithium ion batteries, Electrochimica Acta http://dx.doi.org/10.1016/j.electacta.2017.02.130

Graphene-like carbon sheet/Fe$_3$O$_4$ nanocomposites derived from soda papermaking black liquor for high performance lithium ion batteries

Xinli Yi[a], Wen He[a,b,]*, Xudong Zhang[a,]*, Yuanzheng Yue[b,a,]*, Guihua Yang[c], Zhaoyang Wang[a], Maojuan Zhou[d] and Lianzhou Wang[e,a]

[a]Institute of Materials Science and Engineering, Qilu University of Technology, Jinan 250353, China

[b]Section of Chemistry, Aalborg University, DK-9000 Aalborg, Denmark

[c] Key Laboratory of Pulp and Paper Science and Technology of Ministry of Education, Qilu University of Technology, Jinan 250353, China.

[d] Department of Environmental Science and Engineering, Qilu University of Technology, Jinan 250353, China

[e] Nanomaterials Centre, The School of Chemical Engineering, The University of Queensland, Brisbane, QLD 4072, Australia

*Corresponding author. Tel: +86 18353108836, E-mail: hewen1960@126.com (Wen He) or Tel: +86 89631678, E-mail: zxd1080@126.com (Xudong Zhang) or Tel: +45 96358522, E-mail: yy@bio.aau.dk (Yuanzheng Yue).

Graphical abstract

Highlights

- Lamellar Si/S-in situ doped graphene/Fe_3O_4 nanocomposite were prepared from the soda papermaking black liquor.

- Fe_3O_4 nanoparticles are homogeneously embedded in the interlayer of the lamellar nanocomposite.

- A discharge capacity (3829 mAh g^{-1}) is more than 4 times the theoretical capacity of Fe_3O_4.

- A synergy effect at the nanoscale between different electrochemical reactions.

ABSTRACT

Alkali lignins and its degradation products in the soda papermaking black liquor (SPBL) are renewable resource with the highest natural carbon content. In this work we convert SPBL into the high-performance carbon-based nanocomposite anodes. The unique functional groups of lignin biomass induce spontaneous formation of graphene-like carbon sheet (GCS) in-situ doped SiC/S. The lamellar GCS/Fe_3O_4 nanocomposite (GCS/FO-NC) is facilely prepared via one-step in-situ thermo-chemical method at 700 °C, in which donut shaped Fe_3O_4 nanoparticles with superlattices and inner surface are homogeneously embedded in the interlayer of GCS and are also anchored on its surface. The GCS/FO-NC anode exhibits a ultrahigh first discharge specific capacity of 3829 mAh g^{-1} at 50 mA g^{-1} in a coin-type Li ion battery, which is more than 4 times the theoretical capacity (924 mAh g^{-1}) of Fe_3O_4 and 5 times that of the graphene anode (744 mAh. g^{-1}). Even at a high current density (1000 mA g^{-1}), it still exhibits a high reversible capacity (750 mAh g^{-1}) after 1400 discharge/charge cycles. More importantly, the removal efficiency of chemical oxygen demand of SPBL is up to 83.4% during the synthesis process, which reduce its load to environment and synthetic cost of carbon-based nanocomposite anodes.

1. Introduction

As the world's population continues to grow and does our consumption of natural non-renewable resources, so developing reliable renewable energy sources become increasingly important [1-4]. In abundant renewable lignocellulose, lignin is a highly polymerized material with two-dimensional structure, and is the best carrier of solar energy. Lignin has a higher energy content than cellulose or hemicelluloses. One gram of lignin has on average 2.27 KJ, 30% more than the energy of cellulosic carbohydrate. The energy content of lignin is 15-20 times higher than the yearly output of oil, and the production volume of lignin was about 70 million metric tons per year [5]. However, the lignin is not needed in papermaking process, where it is dissolved from wood chips and become the main component (about 48%) of soda papermarking waste liquor (SPBL) (Fig.1ab). Due to fine particle size of alkali lignin (<500 nm) and suspending particles (<50 nm), high alkalinity (pH=13), high chemical oxygen demand (CODcr) and biological oxygen demand, the recovery of SPBL is expensive and difficult to be biologically treated. So far, the mainstream method to treat SPBL is the industrial combustion. However, this method is not cost-effective because it may cause secondary air pollution [6]. Alkali lignins and its degradation products in SPBL are a renewable resource with the highest natural carbon content, high dispersion and surface activity, which is an ideal precursor for biomass carbon materials. Lignin structure contains different functional groups such as phenolic hydroxyl groups, carboxylic acid groups, sulfonate groups, ether-bridges and methoxyl groups, and trace elements such as Si and S (Fig.1c) [7,8]. These highly

4

hydrophilic groups can provide lone pair electrons and nucleation sites, adsorb metal ions and lead to the cross-linking reaction of lignins to form stable cross-linked structures (Fig.1d,e).

Recently, the renewable biomass-derived porous carbon materials have attracted intensive attention for their possible applications in Li-ion batteries (LIBs) and Na-ion batteries (NIBs) [9-15]. These biomass carbon materials have unique nanostructure, in particular, carbon quantum dots (CQDs,＜10 nm) and nanowires, which differ from those of the nanoparticles derived by other techniques [16,17]. These materials exhibit superior electrochemical performances owing to their high surface area, abundant reactive sites, optimized electronic structure, and fascinating physical and chemical properties. In particular, graphene derived from biomass is a unique and attractive energy material and has provided great opportunity in improving the performances of LIBs and NIBs owing to its excellent electrical conductivity, high mechanical flexibility, large specific surface area, and pronounced thermal and chemical stability [37,38]. Both theoretical calculations and detailed experiments have proven that the intrinsic properties of graphene can be modified by the introduction of heteroatoms, such as sulfur, nitrogen, phosphorus or boron into the carbon frameworks [21-23]. However, the methods used to prepare doped graphene often involve tedious chemical vapor deposition (CVD), plasma treatment, or high temperature annealing methods with high energy consumption and harsh experimental conditions [24]. The composite anode materials of graphene and Fe_3O_4 have been recently explored and show enhanced high capacity and excellent cycling performance of LIBs [25-31]. However,

the Fe_3O_4 nanoparticles one-side lying on the graphene surface would still suffer from the drastic volume expansion and disintegration during the electrochemical processes.

Biorefinery is a new technique, by which biomass, such as the agriculture waste, lignin, starch of plant, lignocellulose can be transformed into various chemicals, bioenergy, biomass graphene, fuel and biomaterials. By this technique we can convert SPBL into the raw materials for fabricating high-performance and low cost electrodes. Herein, we have successfully synthesized the graphene-like carbon sheet (GCS) in-situ doped SiC/S and GCS/Fe_3O_4 nanocomposite (GCS/FO-NC) via a one-step in-situ thermo-chemical method at 700 °C. In the nanocomposite structure, the donut shaped Fe_3O_4 nanoparticles (50-100 nm) with superlattices and inner surface are homogeneously embedded in the interlayer of lamellar GCS. Compared to the reported carbon-based Fe_3O_4 composite [25-31], this nanocomposite has several notable advantages for LIBs and NIBs. First, the flexible GCS (about 33 wt.%) not only offer a stable scaffold for more ion storage sites, ensuring the fast ion transportation and high conductivity, but also provides strain space to buffer the volume expansion/contraction of Fe_3O_4 nanoparticles, sequentially leading to a good cycling stability. Second, the uniform nanogaps (about 3 nm) in GCS make the ions and electrolyte easily penetrate and react with Fe_3O_4, and they could be used as a confining structure with substantial buffering capability to reduce electrode pulverization. Third, due to quantum confinement and size effects, Fe_3O_4 nanoparticles uniformly embedded in the interlayer of GCS guarantee abundant active sites and high interface areas for the insertion/extraction of Li and Na ions and full

6

utilization of the active materials. This is the most significant factor for ultrahigh specific capacity. Owing to these merits, the nanocomposite exhibits completely new electrochemical performances and behavior, which is particularly desirable for high-performance and low cost power batteries in the future. As an additional advantage, this synthesis technology is simple and cost effective. The raw material of GCS is based on abundant renewable resources. More importantly, it can minimize the wast deposition, reduces pollution and greatly enhances battery performances. The removal efficiency of chemical oxygen demand (CODcr) of SPBL is up to 83.4% during the synthesis process (Figs. S1a-c in Supplementary Informationsection). This greatly contributes to reducing the SPBL load to our environment and the synthetic cost of graphene power batteries.

2. Experimental section

2.1. Materials

SPBL from a soda papermaking process (steaming section, ragments of poplar tree as raw material) was obtained from the Shandong Sun Paper Industry Joint Stock Co., Ltd., Yanzhou, China. Ferric chloride hexahydrate ($FeCl_3 \cdot 6H_2O$) and Iron nitrate nonahydrate ($Fe(NO_3)_3 \cdot 9H_2O$, 98%) used in the synthesis process were obtained from commercial sources. Silver sulfate (Ag_2SO_4, 99.5%), standard solution of potassium bichromate (1/6 $K_2Cr_2O_7$, 0.25 mol L^{-1}), Ferroinindicator solution, standard solution of ammonium ferrous sulfate ($Fe(NH_4)_2(SO_4)_2 \cdot 6H_2O$, 0.1mol L^{-1}), Sulfuric acid

(H_2SO_4, 98%), Mercuric sulfate ($HgSO_4$), these chemicals were used for CODcr measurement. All chemicals and materials were used without any further treatment.

2.2. Synthesis of GCS/FO-NC

The nanocomposites were prepared via a carbon thermal reduction technique assisted by hydrothermal method. In the typical process, 30 mL of 1 mol L^{-1} Fe^{3+} solution was slowly dispersed in 50 mL of SPBL drop by drop with magnetic stirring, then stirred at room temperature for 6 h. The pH value of the mixed solution was reduced from 13 to about 7, and then a thick liquid with $Fe(OH)_3$ sediment was obtained. Subsequently, the precursor solution was transferred into a Teflon lined stainless autoclave, and kept at 180 °C for 48 h. After reaction ends, the kettle is naturally cooled to room temperature, and final the product is collected by drying under air at 60 °C. Finally, the resulting samples were calcined at 700 °C in a tube furnace with a heating rate of 5 °C min^{-1} in an nitrogen atmosphere and kept at that temperature for 8 h. Eventually, the nanocomposites were synthesized after being cooled down to room temperature. For comparison, the pure Fe_3O_4 sample (without papermarking waste liquid) and the SPBL ash sample (without Fe^{3+} solution) were applied. More details of material characterization, electrochemical measurements and wastewater characterization can be found in the experimental section of Supporting Information 2. The mass loading of active material in different batteries is show in Table S5.

8

3. Results and discussion

In liquid phase, heterogeneous nucleation occurs much easier at structural inhomogeneities, since active centers with high affinity are already present, the barrier to overcome for nucleation to occur is globally decreased and the nuclei are formed on the first surface of a foreign body [32]. On inhomogeneity substrates, the degree of surface hydrophilicity controlled the rate of nucleation and growth, because increased hydrophilicity can decrease the interfacial energy between the nanoparticles and substrate and improve the nucleation and growth rate of nanoparticles [33]. Lignins with highly hydrophilic groups can provide remarkably reactive sites for heterogeneous nucleation and growth of iron nanoparticles. The recent studies on the heterogeneous nucleation and growth mechanism of iron nanoparticles were carried out, where the orientated attachment of iron at structural inhomogeneities has been viewed with a high resolution transmission electron microscope (HRTEM), and it has been suggested that this attraction is Coulombic attraction in nature and van der Waals interactions [34-36]. Detail TEM investigation in Figs 2ef has also proved that primary iron nanoparticles can adsorb and deposite on GCS to form donut shaped Fe_3O_4 nanoparticles through the heterogeneous nucleation and growth mechanism.

To improve the formation of GCS/FO-NC and reduce the production of volatile, the thermal carbonization was first performed via hydrothermal method. Thermal degradation of various lignins is reported, during which the pyrolysis causes their carbonization, and this is a multistep reaction [37-39]. During hydrothermal reaction, the most of the oxygen functional groups in lignin loss, producing cross-linking

9

between lignin molecules. The reorganization of the structure produces high-ordered carbon materials by condensation of the aromatic rings. Furthermore, the inorganic impurities (mainly Fe) in lignin precursors act as graphitization catalysts and can enhance the onset of structural ordering and induce structural cross-linking, owing to its highly cross-linked nature and the oxidation resistance. These trace elements (Si and S) in lignin structure in situ doped in the cross-linking structure (Fig.1d,e). During carbon thermal reduction reaction, carbonyl, carboxyl and methoxy groups loss and the ordering of the structure is further increased to produce the GCS (Fig. 1f) [39]. The alkali lignin particles in SPBL possess the high dispersibility, cohesiveness, chelating property and hydrophilic behaviour because of a large number of negatively charged functional groups on its surface and electrostatic interactions (Fig.1g). When the Fe^{3+} solution was added to SPBL, the shared pairs of electrons on oxygen atoms of these functional groupseasily combine with Fe^{3+} cations and form the stable lignin chelates by charge neutralization and adsorption bridging action (Fig.1h). Eventually the stratoid precipitation of flocculation body was obtained by chelation effect (Fig.1i). The zeta potential changes of the particle surface determined by using JS94H micro electrophoresis have verified the above conclusion (Fig. S2). The GCS/FO-NC sample was synthesized by hydrothermal and carbon thermal reduction reactions (Fig.1j,k). During pyrolyticdegradation, the stratoid precipitation of lignin chelates is decomposed to form the GCS/FO-NC with robust and effective networks for electron and ion transport. The Fe_3O_4 nanoparticles are homogeneously embedded in the interlayer of GCS and anchored on its surface. The morphology of GCS/FO-NC-D

10

sample was characterized using the high-resolution scanning electron microscopy (SEM). Fig.1l clearly shows that the nanocomposite particles after the calcination have good layer structure, which is favourable to the improvement of electrochemical performance. The large SEM image shows some multi-layer with different thickness and single-layer structures in this product (Fig. S3). It can be observed that the single-layer structure is very abundanted, which is about 10 nm as thick as one layer. The thickness of multi-layer structure is changeable within the scope of 10–150 nm.

Microstructure of the different samples was characterized by SEM and high-resolution TEM (HRTEM). SEM images in Fig.2a and 2b show that the alkali lignin particles in the dry mixture of SPBL form the layer structure by the cross-linking reaction. HRTEM images were obtained at the Scherzer defocus (Δf =-41.25 nm) to optimize the transfer function of the optical system balancing the effect of spherical aberration. According to the image contrast mechanism in the Weak Phase Object (WPO) approximation, HRTEM image formation at a negative Scherzer defocus relies on phase contrast. The phase contrast imaging technique is very sensitive to atomic number. The bigger the atomic number, the darker the WPO image is [54]. Fig. 2c and 2d show some carbon sheets with different sizes in the SPBL ash sample synthesized by carbon thermal reduction reactions at 700 °C. These particles are composed of SiC QDs (＜10 nm), CQDs (＜10 nm) and C nanowire network (Fig.2d). The SiC QDs and CQDs shown in Fig. 2d can be identified as the WPO. SiC atomic columns with bigger atomic number are imaged as darker spots and

11

C atomic columns with smaller atomic number as brighter spots. Fig. 2d shows that the C nanowires with an average size of about 0.5 nm (see the brighter spots followed the white line) interwoven into a network. Fig.2e and 2f show that the donut shaped Fe_3O_4 nanoparticles (dark areas) with a diameter of 50-100 nm and width of about 20 nm are homogeneously embedded in a GCS (grey area) and anchored on its surface, in good a greement with the XRD results (Fig.3aB). The Fe_3O_4 nanoparticles are sandwiched between the GCSs, resulting in a larger interlayer space of nanocomposite. It is found that there are many CQDs (yellow circles) with high conductivity and nanogaps (white areas) with good permeability of the ions and electrolyte in Fe_3O_4 nanoparticle (Fig.2g). More direct evidence for Fe_3O_4 crystal structure is seen in Fig.2g, showing the well-identified Fe_3O_4 (311) lattice fringes with a smaller d-spacing of 0.252 nm [28]. Also the HRTEM image (Fig. 2h) of an individual Fe_3O_4 nanoparticle displays its superlattice structure with a larger lattice spacing of 0.98 nm [41]. Fig. 2i is a schematic illustration of the formation of Fe_3O_4 super lattices by using lignins as structral templates and proposed lithium storage by intercalation into the quantum wells of superlattice structure. In the synthesis, lignin template can

influence the nucleation and growth of Fe_3O_4 nanoparticle, and control their microstructure. It has recently been demonstrated that the superlattice structure has abundant reactive sites of Li^+, optimized electronic structure, and fascinating physical and chemical properties, which can enhance the efficient charge transfer and the kinetics of electron and ion transport due to quantum confinement and size effects

12

[41]. Fig. 2j-m show the elemental mapping images of Fe, C, Si and S in the GCS/FO-NC-D sample. And all the elements originating from papermarking black liquor except Fe. The results show the uniformly dispersed of Fe, C, Si and S in GCS/FO-NC-D sample. It is evident that the Fe_3O_4 nanoparticles were uniformly dispersed in the GCS without agglomeration, which is beneficial to buffer volume change of Fe_3O_4 nanoparticles during the lithium-ion insertion/extraction process, making a contribution to improve the electrochemical performance of the composite.

Fig. 3aA is the XRD pattern of the SPBL ash sample synthesized without adding ferric salt, showing two broad diffraction peaks of carbon nanosheets centered at 22.5 and 43.1° [22-31] and the diffraction peaks of β-SiC (PDF#49-1623) with a cubic crystal system [42]. The broad peak indicates that its structure has a high degree of disorder. The content of carbon nanosheets and β-SiC is about 61 and 39% by calculating their intensity ratio of characteristic diffraction peaks, respectively. This result indicates that the structure and components of lignin particles in SPBL facilitate the in-situ synthesizing of carbon nanosheets and β-SiC at lower temperature (700 °C). In addition, the carbon nanosheet structure of the SPBL ash sample has also been confirmed by Raman spectrum (Fig.3bA) and HRTEM images (Fig.2c,d). Fig.3aB and Fig. S4a show the diffraction peaks of the GCS/FO-NC-D sample, which can be well indexed to the cubic phase of magnetite (Fe_3O_4) with Fd3m space group (PDF#88-0315), carbon nanosheet and trace amounts of Fe (PDF#99-0064). To determine the elemental content and distributions of the GCS/FO-NC-D sample, quantitative analysis has been performed using the energy-dispersive spectrometry

13

(EDS) (Fig.3g). The computed results indicate that the molar ratio of Fe_3O_4:Fe: C:S:SiC:Na is about 2.0:0.1:27.0:0.41:0.53:0.91 in the GCS/FO-NC-D sample. As seen in Fig.3g, the content of Si and S is very limited. The content of SiC is 4.34 wt.%, measured with Gravimetric method. The weak peaks in Fig.3aC indicate that the hydrothermal process is beneficial to the nucleation and growth of Fe_3O_4. Fig.3aD showsthe XRD pattern of the blank sample synthesized without adding SPBL by hydrothermal reaction, exhibiting the diffraction peaks of Fe_3O_4, FeO (PDF#89-2468) and Fe. A comparison with Fig.3aD shows that the weaker peak at 45° in Fig.3aB can be attributed to the (110) plane of Fe phase [43], indicating that a trace amount of ferrous iron was reduced into metallic iron, which is conducive to the one-step in-situ synthesis of carbon nanosheets [44]. The weaker broad bump in the 2 θ range of 5 to 11.5° in Fig.S4a further confirms the Fe_3O_4 super lattice structure in Fig.2h. The strong broad bump in the 2 θ ranges of 11.5 to 22.5° can be ascribed to the large amounts of carbon nanosheets (about 33 wt.%) and the lamellar structure of GCS in the GCS/FO-NC-D sample (further validated the SEM in Fig.1i).

Raman spectra of the SPBL ash sample in Fig3bA show three strong characteristic peaks of carbon nanosheets, centered at 1346.7, 1593.3 and 2900 cm^{-1} and corresponding to the D, G, and 2D band, respectively [21,45]. The intensity ratio (I_D/I_G) of D-band to G-band is 0.92, indicating the high quality and ordering degree of the GCS structure. By comparing with Fig.3bA, it is found that although the peak positions of three characteristic peaks of carbon nanosheets in Fig.3bB have not shifted, their intensities significantly decreases and I_D/I_G was increased to 0.95. These

14

changes indicate that the local structure of carbon nanosheets in the GCS/FO-NC-D sample has not changed, but the degree of the long range disorder increases due to the intervention of Fe_3O_4 nanoparticles and the introduction of more defects [21].

Similarly, Fourier Transform Infrared Spectroscopy (FTIR) analysis also confirm the composite structure of Fe_3O_4 with GCS (Fig. S4b). The results were further confirmed by HRTEM images (Fig.2e-h). Fig.3cd show a surreyspectrum of X-ray photoelectronspectroscopy (XPS) for the GCS/FO-NC-D sample. There are four main peaks in Fig.3c, indicating the presence of C, Na, O elements and Cl impurity. However, the signal strength of Fe element is very weak because the Fe_3O_4 particles in GCS/FO-NC-D were completely embedded in the interlayer of GCS [21]. The spectrum of Fe $2p_{3/2}$ and $2p_{1/2}$, is shown in Fig.3d and the spectra of O 1s and C 1s are shown Fig.S4c and S4d, respectively. The XPS results further validate the XRD results in Fig.3aB. The porous structure of the different samples were characterized by N_2 adsorption/desorption isotherms, as shown in Fig.3ef. Only the GCS/FO-NC-D sample exhibits a H4-type hysteresis loop of type V isotherm with uniform mesoporous structure (Fig.3eB). The size of slit pores and BET specific surface area are about 3 nm and 258.7 m^2g^{-1}, respectively. The summary of the structural features and performances of the synthesized samples are shown in supplementary Table S2. The higher BET surface and uniform mesoporous structure can promote the permeability of electrolyte, resulting in an excellent electrochemical performance.

Biomass graphene or carbon sheets from biomass resources are an appealing

two-dimensional material with superior electrochemistry properties because of its ultrathin nanosheet frameworks (2–10 atomic layers) and the mesoporous structure [45,46]. In this study, we have also synthesized GCS with graphene-like structure via a simple thermo-chemical method. The galvanostatic charge/discharge and cyclic voltammetry (CV) profilesof the different electrodes were shown in Fig.4. When used as an anode material for LIBs, the GCS delivers a high reversible capacity of 1058 mAh g^{-1} at 50 mAh g^{-1} (Fig.4a), which is higher than the maximum theoretical specific capacity of the graphene anode (744 mAh. g^{-1}). Fig.4a only shows an unconspicuous discharge plateau around 0.1 V. The CV curves in the first three cycles almost overlapped, indicating its good reversibility (Fig.4b). Compared with the blank electrode (Fig.4c), it is found that the GCS/FO-NC-D anode exhibits a ultrahigh first discharge specifi ccapacity of 3829 mAh g^{-1} and a charge specific capacity of 2250 mAh g^{-1} at 50 mA g^{-1} (Fig.4e), which is far higher than the theoretical capacity of Fe_3O_4 anode (924 mAh g^{-1}). But it rapidly decay to 2373 mAh g^{-1} after 3 cycles, which refers to the presence of some irreversible reactions and the formation of solid electrolyte interface (SEI) film [47]. The CV profiles of the blank electrode in Fig.4d show two sharper peaks at about 0.7–0.9 and 1.7–1.8V, corresponding to the electrochemical reduction/oxidation reactions ($Fe^{3+} \leftrightarrow Fe^0$) and accompanying with the insertion/extraction of lithium-ion [48]. However, the new peaks at about 0.59, 1.6 and 2.2 V appear in the GCS/FO-NC-D anode (Fig.4f), which can be accounted by the electrochemical reduction/oxidation reactions of SiC/S doped phases [22,24,42]. Note that both the cathodic and the anodic peaks of Fe_3O_4 in GCS/FO-NC-D have a

pronounced shift compared to the blank electrode (Fig.4d), meaning that the GCS can facilitate the electrochemical reduction/oxidation reactions of Fe_3O_4. It is noteworthy that the intensity of both cathodic and anodic peaks in Fig.4f has significantly increased, implying that the GCS can also improve energy density. This result has been proven by Fig.4g, exhibiting a ultrahigh charge energy density of 2625 Wh kg^{-1} and a discharge energy density of 1250 Wh kg^{-1} at 50 mA g^{-1} after three cycles. The optimum compositions of the GCS/FO-NC-D for LIB/NIB applications show in Figure S1d and Table S1, respectively. The results show that the Li/Na-storage properties of the GCS /FO-NC-D can be improved by incorporating suitable carbon networks/heteroatoms doping. But the theoretical capacity of composite will be reduced in the too high carbon content. The SC/S-GNCs/FO-NC-D sample has the optimum molar ratio of Fe_3O_4:Fe:C:S:SiC:Na, which is about 2.0:0.1:27.0:0.41:0.53:0.91.

These superior electrochemical performances of the GCS/FO-NC-D anode can be attributed to the collective and synergetic effects at the nanoscale between different electrochemical reactions in the GCS/FO-NC-D anode, as shown in Fig.5. The traditional Fe_3O_4/CN composite (Fig5a) and the GCS (Fig5b) have a low Li storage because of lack of inner surface, but the GCS/FO-NC-D anode can provide a high Li storage and much larger atomic interface contact because of inner surface in the donut shaped Fe_3O_4 nanoparticle with super-lattice structure and interaction between donut shaped Fe_3O_4 nanoparticles and GCS (Fig5 c). Fig5 de show schematic of the phase reactions of Fe_3O_4 spheroidal particle (Fig5 d) and donut shaped Fe_3O_4

17

nanoparticle with the inner surface (Fig5 e) during lithiation, exhibiting the different pathway of electron transport at the particle surface. The donut shaped Fe_3O_4 embedded in the interlayer of GCS not only have abundant reactive sites for Li storage and optimized electronic structure for charge transfer, but also could provide a large electrode/electrolyte interface area and the fast diffusion path of lithium ions and electrons. Besides highly stable GCS in GCS/FO-NC structure also play an important role in enhancing the capacity performance of the nanocomposite electrode. First, its high conductivity, the GCS can also serve as a stable scaffold for more ion storage sites, the high conductive medium for ensuring the fast ion transportation and elastic buffer of volume change for the Fe_3O_4 nanoparticles. Second, the uniform nanogap structure in GCS can make the ions and electrolyte easily penetrate and react with Fe_3O_4 to reduce electrode pulverization. Third, due to quantum confinement and size effects SiCQDs, CQDs, carbon nanowires and heteroatoms doping in in GCS, the electrodes exhibit superior electrochemical performances owing to their high surface area, abundant reactive sites, optimized electronic structure, and fascinating physical and chemical properties. Silicon carbide (SiC) and sulfur-doped carbon have recently been found to be potential high-performance anode materials upon activation by surface graphitization due to its superior high-rate performance and cycling stability [42,48]. But most of all, the electrochemical reactions of the different phases in GCS/FO-NC structure have the collective and synergetic effect, leading to a ultrahigh reversible specific capacity and the excellent rate capability and cycling stability of the nanocomposite electrode. The possible Li^+ ion insertion/extraction mechanism of

18

GCS/FO-NC as anode for LIBs can be described as follows:

$$Fe_3O_4 + 8e^- + 8Li^+ \leftrightarrow 3Fe + 4Li_2O \tag{1}$$

$$6C + Li^+ + e^- \leftrightarrow LiC_6 \tag{2}$$

$$[SiC]^{4-} + 4Li^+ \leftrightarrow Li_4[SiC] \tag{3}$$

$$S + 2Li^+ + 2e^- \leftrightarrow Li_2S \tag{4}$$

The rate capability and cycling stability of different electrodes are also evaluated by charge/discharge test at various current densities. Fig6 shows the rate capability and corresponding Coulombic efficiency of the GCS/FO-NC-D anode and the GCS/FO-NC-D sample synthesized by repeated tests at various current densities. After 70 cycles at varied current rates from 100 to 1000 mA g^{-1} for the two cycles, both the GCS/FO-NC-D anode (Fig6a) and the GCS/FO-NC-D sample synthesized by repeated tests (Fig6b) delivered a high discharge capacity of about 570 mAh g^{-1} and an ultra-high Coulombic efficiency close to 98%. Compared with the SPBL ash

and Fe_3O_4/FeO/Fe blank sample (Fig S5), it is found that the GCS/FO-NC-D anode shows better high rate performance. After 50 cycles at varied current rates from 1000 to 10000 mA g^{-1} for a cycle, the GCS/FO-NC-D sample synthesized by repeated tests still delivered a high discharge capacity of 235 mAh g^{-1}, showing outstanding high rate capability (Fig6c).

Most notably, the GCS/FO-NC-D electrode also has excellent cycle stability and good Coulombic efficiency even at a high current density of 1000 mA g^{-1} (Fig 7a). Its initial discharge sepcific capacity is up to 1385.2 mAh g^{-1}, which is almost 4 times the

capacity of a commercial graphite anode (372 mAh/g), and is the highest rate capability compared with those reported in the literature [27-31, 50-53]. And it still exhibits a high reversible capacity (750 mAh g^{-1}) after 1400 discharge/charge cycles. In addition, its Coulomb efficiency is close to 100% after 3 cycles and can be maintained indefinitely, indicating the outstanding and effective processes of charging and discharging. It's worth noting that in the cycling process the reversible capacity reduced obviously before 100 cycles and then remained at about 320 mAh g^{-1} from 100th up to 700th cycle. The reversible capacity lossas increasing crycling number may be ascribed to many factors, such as the formation of inorganic solid electrolyte interface (SEI) film, the change of nanostructure, the degradation of the lithium metal foil cathode and so on [54]. Here, the experimental temperature is suggested to be mainly responsibly for reducing the capacity. The lower capacity at the average temperature of -10 °C is due to the increase in viscosity and resistance of the electrolyte, the decrease in penetrability of the electrolyte, and the increase of the activation energy for lithium-ion diffusion and intercalation, which decreased its active surface area and limited lithium storage sites [55-57]. The cyclic voltammogram (CV) and electrochemical impedance spectroscopy (EIS) performances of this electrode at different crycling number are measured as shown in (FigS6), which can help to clarify the ohmic resistance and polarization resistance behaviors coincident with capacity loss. But surprisingly, as the temperature is elevated to 10 °C, the capacity of GCS/FO-NC-D anode begins to increases significantly after 700 cycles and increase to the highest capacity of 750 mAh g^{-1} after

1400 cycles. This increasing phenomenon is attributed to three main possibilities as follows. Firstly, as crycling number and room temperature incrase, the viscosity and resistance of the electrolyte decreases, which make the ions and electrolyte more easily penetrate in the uniform nanogaps (3 nm) of GCS and react with Fe_3O_4 nanoparticles. Secondly, the more ion storage sites and electron reactions in GCS/FO-NC may be reactivated and released by crycling electrochemical reactions. Third, the charge and discharge increased the active surface area of Fe_3O_4 nanoparticles and lithium metal cathode, which provides more active sites for additional Li storage. In a word, this is attributed to the excellent nanocomposite structure of Fe_3O_4 nanoparticles embedded inside the lamellar structure of GCS.

To optimize synthesis conditions, the electrochemical performances of the different nanocomposite electrodes synthesized with different annealing temperature are shown in Fig 7b and Table S4. The results show that the composite electrode synthesized at 700°C for LIBs has not only high initial discharge capacity and coulombic efficiency (Table S4), but also better cycle performance than that of the electrodes synthesized at 600 and 800 °C. However, the Coulombic efficiency of all the samples are maintained at about 100%, suggesting the effectively reversible lithiation/delithiation process. The improved performances are originated from the nanocomposite structure of GCS and Fe_3O_4 nanoparticles and the incorporation of suitable carbon networks/heteroatoms doping. Especially GCS not only offer a stable scaffold for more ion storage sites, facilitates the Li^+ delithiation/lithiation, accordingly increasing the discharge capacity and initial coulombic efficiency, also

21

provides strain space to buffer the volume expansion/contraction of Fe_3O_4 nanoparticles, sequentially leading to a good cycling stability. This offers a new insight for simultaneously increasing the initial coulombic efficiency and the specific capacity for LIBs.

To further investigate its multifunctional applications, the cycling performance and Coulombic efficiency of GCS/FO-NC-D anode for different batteries at 50 mA g^{-1} up to 100cycles were also shown in Fig 7c. The initial discharge specific capacities are 2755.2 mAh g^{-1}, 2167.2 mAh g^{-1} and 1040.7 mAh g^{-1} with 71.5%, 60.0% and 67.0% coulombic efficiency for LIBs, NLHBs and NIBs, respectively. By contrast, it is found that the lithium-ion battery assembled with the lamellar nanocomposite as an anode exhibits high reversible capacity and better cycling stability than that of NLHBs and NIBs after 100 discharge/charge cycles, and the Coulomb efficiency of the LIBs, NLHBs and NIBsis all close to 100% after 100 cycles. But the reversible capacity and cycling stability of NIBs need to be improved.

4. Conclusions

In summary, by the soda papermarking waste liquor (SPBL) as template and raw materials, we successfully fabricated graphene-like carbon sheet (GCS) in-situ doped SiC/S and GCS/Fe_3O_4 nanocomposite (GCS/FO-NC) with high capacities, long cycling lives, and good rate performances. The formation mechanism and the possible Li$^+$ ion insertion/extraction mechanism of the GCS and GCS/FO-NC were discussed.

Their structure, composition and electrochemical performances were analyzed and characterized. The analysis results show that the functional groups and the properties of alkali lignin biomass in SPBL play an important role in the formation of the GCS and GCS/FO-NC. In the GCS/FO-NC structure, the donut shaped Fe_3O_4 nanoparticles with superlattices and inner surface are homogeneously embedded in the interlayer of GCS with the uniform nanogaps (about 3 nm) and anchored on its surface. The molar ratio of Fe_3O_4:C in GCS/FO-NC is about 2:27. In comparison to the composites of graphene extracted from graphite with Fe_3O_4, GCS/FO-NC can significantly improve electrochemical properties of LIBs and NIBs because of its unique nanostructure and the collective and synergy effects between different electrochemical reactions. The GCS/FO-NC anode exhibits a ultrahigh first discharge specific capacity of 3829 mAh g^{-1} and a charge specific capacity of 2250 mAh g^{-1} at 50 mA g^{-1} in a coin-type Li ion battery, which is more than 4 times the theoretical capacity (924 mAh g^{-1}) of Fe_3O_4 anode. In addition, this approach is simple and cost-effective for reducing the waste water pollution and for developing high-performance power batteries. We foresee that our work may have an impact in the fields of environmental science, materials science, energy technology and bionanotechnology.

Author contributions

W.H., X.Z. and Y.Y. conceived and designed the experiments; X.Y. and Z.W. performed the experiments and electrochemical measurements; G.Y., M.Z. and L.W. assisted in the experiments of materials characterization; W.H., X.Z. and Y.Y. co-wrote the paper. All authors discussed the results and commented on the manuscript.

Acknowledgements

Appendix A. Supporting information

Supplementary data associated with this article can be found in the online version at http://dx.doi.org/

References

[1] S.P. Leitner, C. Paulik, H. Weber, G. Gratzl, Carbon Materials from Lignin and Sodium Lignosulfonate via Diisocyanate Cross-Linking and Subsequent Carbonization, Carbon 1 (1) (2015)43–57.

[2] D Cai, D Li, LX Ding, S Wang, H Wang, Interconnected α-Fe2O3 nanosheet arrays as high-performance anode materials for lithium-ion batteries, Electrochimica Acta 192 (2016) 407–413.

[3] K Lu, J Xu, J Zhang, B Song, H Ma, General preparation of three-dimensional porous metal oxide foams coated with nitrogen-doped carbon for enhanced lithium storage, ACS Appl. Mater. Interfaces 8 (2016) 17402–17408.

[4] Z. Zhao, F.S. Cannon, C. Nieto-Delgado, L. Pena, Lignin/collagen hybrid biomaterials as binder substitute for specialty graphites and electrodes, Carbon, 108 (2016) 303–317.

[5] Z. Hu, Y. Que, Y. Gao, Y. Yin, Y. Zhao, Using Black Liquor from the Soda Pulping Process for Protein Production by Candida utilis, Bioresources 10 (3)(2015) 3908–3921.

[6] A.J. Ragauskas, G.T. Beckham, M.J. Biddy, R. Chandra, F. Chen, M.F. Davis, B.H. Davison, R.A. Dixon, P. Gilna, M. Keller, P. Langan, A.K. Naskar, J.N. Saddler, T. J. Tschaplinski, G.A. Tuskan, C.E. Wyman, Lignin valorization: improving lignin processing in the biorefinery, Science 344(6185) (2014) 1246843.

[7] S. Laurichesse, L. Avérous, Chemical modification of lignins: Towards biobased polymers, Progress in Polymer Science 39(7) (2014) 1266–1290.

[8] W. Liu, R. Zhou, D. Zhou, G. Ding, J.M. Soah, C.Y. Yue, X. Lu, Lignin-assisted direct exfoliation of graphite to graphene in aqueous media and its application in polymer composites, Carbon 83 (2015) 188–197.

[9] D. Larcher, J.M. Tarascon, Towards greener and more sustainable batteries for electrical energy storage, Nat. Chem. 7(1)(2015)19–29.

[10] J. Ou, Y. Zhang, L. Chen, Q. Zhao, Y. Meng, Y. Guo, D. Xiao, Nitrogen-rich porous carbon derived from biomass as a high performance anode material for lithium ion batteries, J. Mater. Chem. A 3(12)(2015) 6534–6541.

[11] F. Chen, J. Yang, T. Bai, B. Long, X. Zhou, Facile synthesis of few-layer graphene from biomass waste and its application in lithium ion batteries, J. Electroanal. Chem. 768 (2016)18–26.

[12] X. Yu, K. Zhang, N. Tian, A. Qin, L. Liao, R. Du, C. Wei, Biomass carbon derived from sisal fiber as anode material for lithium-ion batteries, Materials Letters 142(2015) 193–196.

[13] T. Yang, T. Qian, M. Wang, X. Shen, N. Xu, Z. Sun, C. Yan, A sustainable route from biomass byproduct okara to high content nitrogen-doped carbon sheets for efficient sodium ion batteries, Adv. Mater. 28(3)(2016) 539–545.

[14] X. Zhou, F. Chen, T. Bai, B. Long, Q. Liao, Y. Ren, J. Yang, Interconnected highly graphitic carbon nanosheets derived from wheat stalk as high performance anode materials for lithium ion batteries, Green Chemistry 18(7)(2016) 2078–2088.

[15] X. Li, M. Rui, J. Song, Z. Shen, H. Zeng, Carbon and graphene quantum dots for optoelectronic and energy devices: a review, Adv. Funct. Mater. 25(31)(2015) 4929–4947.

[16] H. Hou, C.E. Banks, M. Jing, Y. Zhang, X. Ji, Carbon quantum dots and their derivative 3D

26

porous carbon frameworks for sodium-ion batteries with ultralong cycle life, Adv. Mater. 27(47)(2015) 7861–7866.

[17] L. Mai, X. Tian, X. Xu, L. Chang, L. Xu, Nanowire Electrodes for Electrochemical Energy Storage Devices, Chem. Rev. 114(23)(2014)11828–11862.

[18] G.Y. Xu, J.P. Han, B. Ding, P. Nie, J. Pan, H. Dou, H.S. Li, X.G. Zhang, Biomass-derived porous carbon materials with sulfur and nitrogen dual-doping for energy storage, Green Chemistry 17(3)(2015)1668–1674.

[19] Y. Zuo, G. Wang, J. Peng, G. Li, Y. Ma, F. Yu, B. Dai, X. Guo, C.P. Wong, Hybridization of graphene nanosheets and carbon-coated hollow Fe_3O_4 nanoparticles as a high-performance anode material for lithium-ion batteries, J. Mater. Chem. A 4(7)(2016) 2453–2460.

[20] F. Zhang, T. Zhang, X. Yang, L. Zhang, K. Leng, Y. Huang, Y.S. Chen, A high-performance supercapacitor-battery hybrid energy storage device based on graphene-enhanced electrode materials with ultrahigh energy density, Energy Environ. Sci. 6(5)(2013)1623–1632.

[21] J. Guo, H. Zhu, Y. Sun, X. Zhang, Construction of sandwiched graphene paper@Fe_3O_4 nanorod array@graphene for large and fast lithium storage with an extended lifespan, J. Mater. Chem. A3 (38) (2015) 19384–19392.

[22] S Xin, YG Guo, LJ Wan, Nanocarbon networks for advanced rechargeable lithium batteries, Acc. Chem. Res. 45 (2012) 1759–1769.

[23] M.A. Hoque, F.M. Hassan, M.-H. Seo, J.-Y. Choi, M. Pritzker, S. Knights, S.Y. Ye, Z.W. Chen, Optimization of sulfur-doped graphene as an emerging platinum nanowires support for oxygen reduction reaction, Nano Energy 19 (2016) 27–38.

[24] Z.L. Ma, S. Dou, A.L. Shen, L. Tao, L.M. Dai, S.Y. Wang, Sulfur-doped graphene derived

from cycled lithium-sulfur batteries as a metal-free electrocatalyst for the oxygen reduction reaction, Angew. Chem. Int. Ed. 54(6)(2015) 1888–1892.

[25] Z. Zhang, F. Wang, Q. An, W. Li, P. Wu. Synthesis of graphene@Fe_3O_4@ C core–shell nanosheets for high-performance lithium ion batteries, J. Mater. Chem. A 3 (13) (2015) 7036–7043.

[26] J. Jiao, W. Qiu, J. Tang, L. Chen, L. Jing, Synthesis of well-defined Fe_3O_4 nanorods/N-doped graphene for lithium-ion batteries, Nano Research 9 (5) (2016) 1256–1266.

[27] G. Zhou, D.W. Wang, F. Li, L. Zhang, N. Li, Z.S. Wu, L. Wen, G.Q. Lu, H.M. Cheng, Graphene-wrapped Fe_3O_4anode material with improved reversible capacity and cyclic stability for lithium ion batteries, Chem.Mater. 22 (18) (2010) 5306–5313.

[28] J. Luo, J. Liu, Z. Zeng, F.N. Chi, L. Ma, H. Zhang, J.Y. Lin, Z.X. Shen, H.J. Fan, Three-dimensional graphene foam supported Fe_3O_4 lithium battery anodes with long cycle life and high rate capability, Nano Letters 13 (12) (2013) 6136–6143.

[29] L. Zhao, M. Gao, W. Yue, Y. Jiang, Y. Wang, Y. Ren, F.Q. Hu, Sandwich-structured graphene-Fe_3O_4@carbon nanocomposites for high-performance lithium-ion batteries, ACS Appl. Mater. Interfaces 7(18) (2015) 9709–9715.

[30] P Lian, S Liang, X Zhu, W Yang, H Wang, A novel Fe_3O_4–SnO_2–graphene ternary nanocomposite as an anode material for lithium-ion batteries, Electrochimica Acta 58 (2011) 81–88.

[31] P Lian, X Zhu, H Xiang, Z Li, W Yang, H Wang, Enhanced cycling performance of Fe_3O_4–graphene nanocomposite as an anode material for lithium-ion batteries, Electrochimica Acta 56 (2010) 834–840.

[32] N.T.K. Thanh, N. Maclean, S. Mahiddine, Mechanisms of Nucleation and Growth of Nano-particles in Solution, Chem. Rev. 114 (2014) 7610−7630.

[33] Y.S. Jun, D. Kim, C.W. Neil, Heterogeneous Nucleation and Growth of Nanoparticles at Environmental Interfaces, Acc. Chem. Res. 49 (2016) 1681−1690.

[34] D. Li, M.H. Nielsen, J.R.I. Lee, C. Frandsen, J.F. Banfield, Y. De, Direction-Specific Interactions Control Crystal Growth by Oriented Attachment, J. J. Science 336 (2012) 1014−1018.

[35] Ronghua Wang, Chaohe Xu, Jing Sun, Lian Gao, Three-Dimensional Fe_2O_3 Nanocubes/Nitrogen-doped Graphene Aerogels:Nucleation Mechanism and Lithium Storage Properties, Scientific Reports 4 (2014) 7171−7178.

[36] X.D. Zhang, W. He, Y.Z. Yue, R.M. Wang, J.X. Shen, S.J. Liu, J.Y. Ma, M. Li, F.X. Xu, Bio-synthesis participated mechanism of mesoporous $LiFePO_4/C$ nanocomposite microspheres for lithium ion battery, J. Mater. Chem. 22 (2012) 19948−19956,

[37] Q. Liu, S. Wang, Y. Zheng, Z. Luo, K. Cen, Mechanism study of wood lignin pyrolysis by using TG–FTIR analysis, J. Anal. Appl. Pyrolysis 82 (1) (2008) 170–177.

[38] M. Brebu, T. Tamminen, I. Spiridon, Thermal degradation of various lignins by TG-MS/FTIR and Py-GC-MS, J. Anal. Appl. Pyrolysis 104 (11) (2013) 531–539.

[39] B. Li, W. Lv, Q. Zhang, T. Wang, L. Ma, Pyrolysis and Catalytic Pyrolysis of Industrial Lignins by TG-FTIR: Kinetics and Products, J. Anal. Appl. Pyrolysis108 (7) (2014) 295–300.

[40] Y. Jiao, D. Han, L. Liu, L. Ji, G. Guo, J. Hu, D. Yang, A. Dong, Highly Ordered Mesoporous Few-Layer Graphene Frameworks Enabled by Fe_3O_4 Nanocrystal Superlattices, Angew. Chem. Int. Ed. 127 (19) (2015) 5819–5823.

[41] Y Jiao, D Han, Y Ding, X Zhang, G Guo, J Hu, D. Yang, A. Dong, Fabrication of three-dimensionally interconnected nanoparticle superlattices and their lithium-ion storage properties, Nat. Commun. 6 (2015) 6420–6428.

[42] H. Li, H. Yu, X. Zhang, G. Guo, J. Hu, A. Dong, D. Yang, Bowl-like 3C-SiC nanoshells encapsulated in hollow graphitic carbon spheres for high-rate lithium-ion batteries, Chem. Mater. 28 (2016) 1179–1186.

[43] S. Zhang, W. He, X. Zhang, G. Yang, J. Ma, X. Yang, X. Song, Fabricating Fe_3O_4 /Fe/Biocarbon Fibers using Cellulose Nanocrystals for High-Rate Li-ion Battery Anode, Electrochimica Acta 174 (2015) 1175–1184.

[44] Z.J. Fan, W. Kai, J. Yan, T. Wei, L.J. Zhi, J. Feng, Y. Ren, L.P. Song, F. Wei, Facile synthesis of graphene nanosheets via Fe reduction of exfoliated graphite oxide, ACS Nano 5 (1) (2011) 191–198.

[45] A. Primo, P.Atienzar, E. Sanchez, J. Delgadob, H.García, From biomass wastes to large-area, high-quality, N-doped graphene: catalyst-free carbonization of chitosan coatings on arbitrary substrates, Chem. Commun. 48 (74) (2012) 9254–9256.

[46] F. Chen, J. Yang, T. Bai, B. Long, X. Zhou, Facile synthesis of few-layer graphene from biomass waste and its application in lithium ion batteries, J. Electroanal. Chem. 768 (2016) 18–26.

[47] F. Wu, R. Huang, D. Mu, B. Wu, S. Chen, New synthesis of a foamlike Fe_3O_4/C composite via a self-expanding process and its electrochemical performance as anode material for lithium-ion batteries, ACS Appl. Mater. Interfaces 6 (21) (2014) 19254−19264.

[48] J. Su, M. Cao, L. Ren, C. Hu, Fe_3O_4–graphene nanocomposites with improved lithium

storage and magnetism properties, J. Phys. Chem. C 115 (30) (2011) 14469–14477.

[49] W. Li, M. Zhou, H. Li, K. Wang, S. Cheng, K. Jiang, A high performance sulfur-doped disordered carbon anode for sodium ion batteries, Energy Environ. Sci. 8 (10) (2015) 2916–2921.

[50] J. Zhang, K. Wang, Q. Xu, Y. Zhou, F. Cheng, S. Guo, Beyond yolk-shell nanoparticles: $Fe_3O_4@Fe_3C$ core@shell nanoparticles as yolks and carbon nanospindles as shells for efficient lithium ion storage, Acs Nano 9 (3) (2015) 3369–3376.

[51] H. Zhang, L. Zhou, O. Noonan, D.J. Martin, A.K. Whittaker, C. Yu, Tailoring the void size of iron oxide@carbon yolk-shell structure for optimized lithium storage, Adv. Funct. Mater. 24 (27) (2014) 4337–4342.

[52] E. Kang, Y.S. Jung, A.S. Cavanagh, G.H. Kim, S.M. George, A.C. Dillon, J.K. Kim, J. Lee, Fe_3O_4nanoparticles confined in mesocellular carbon foam for high performance anode materials for lithium-ion batteries, Adv. Funct. Mater. 21 (13) (2011) 2430–2438.

[53] C. He, S. Wu, N. Zhao, C. Shi, E. Liu, J. Li, Carbon-encapsulated Fe_3O_4nanoparticles as a high-rate lithium ion battery anode material, Acs Nano 7 (5) (2013) 4459–4469.

[54] X. Zhang, Z. Bi, W. He, G. Yang, H. Liu, Y. Yue, Fabricating high-energy quantum dots in ultra-thin $LiFePO_4$ nanosheets using a multifunctional high-energy biomolecule—ATP, Energy Environ. Sci. 7 (7) (2014) 2285–2294.

[55] X. Sun, X.Zhang, K.Wang, N.Xu, Y. Ma, Temperature effect on electrochemical performances of Li-ion hybrid capacitors, J. Solid State Electr. 19 (8) (2015) 2501–2506.

[56] R. Wang, X. Li, Z. Wang, H. Guo, J.Wang, Electrochemical analysis for cycle performance and capacity fading of lithium manganese oxide spinel cathode at elevated temperature using

p-toluenesulfonyl isocyanate as electrolyte additive, Electrochimica Acta 180 (2015) 815–823.

[57] S Yuan, J. Li, L. Yang, L. Su, L. Liu, Z. Zhou, Preparation and lithium storage performances of mesoporous Fe_3O_4@ C microcapsules, ACS Appl. Mater. Interfaces 3 (3) (2011) 705–709.
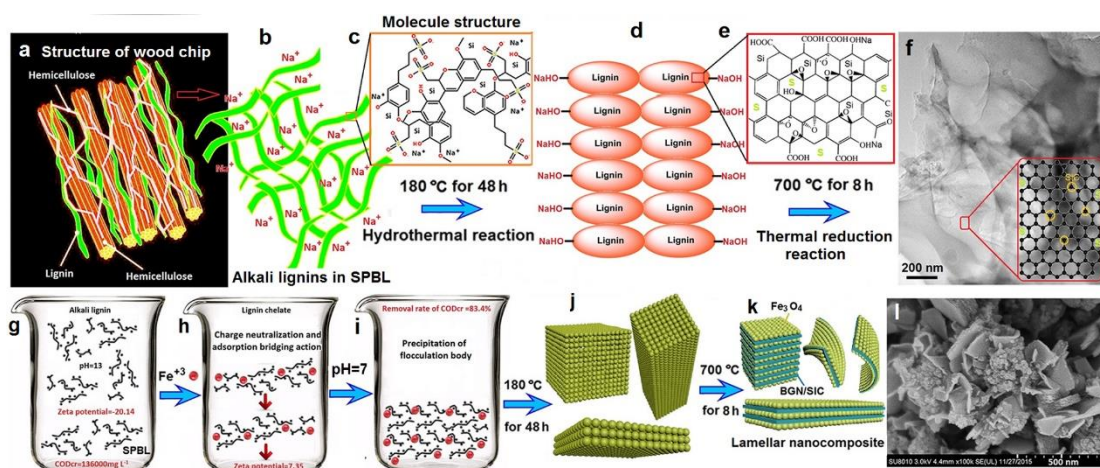
Fig. 1 Fabrication procedure. (a-f) Schematic illustration for the fabrication of GCS. (g-k) Schematic illustration for the fabrication of GCS/FO-NC. (l) SEM image of GCS/FO-NC-D sample.
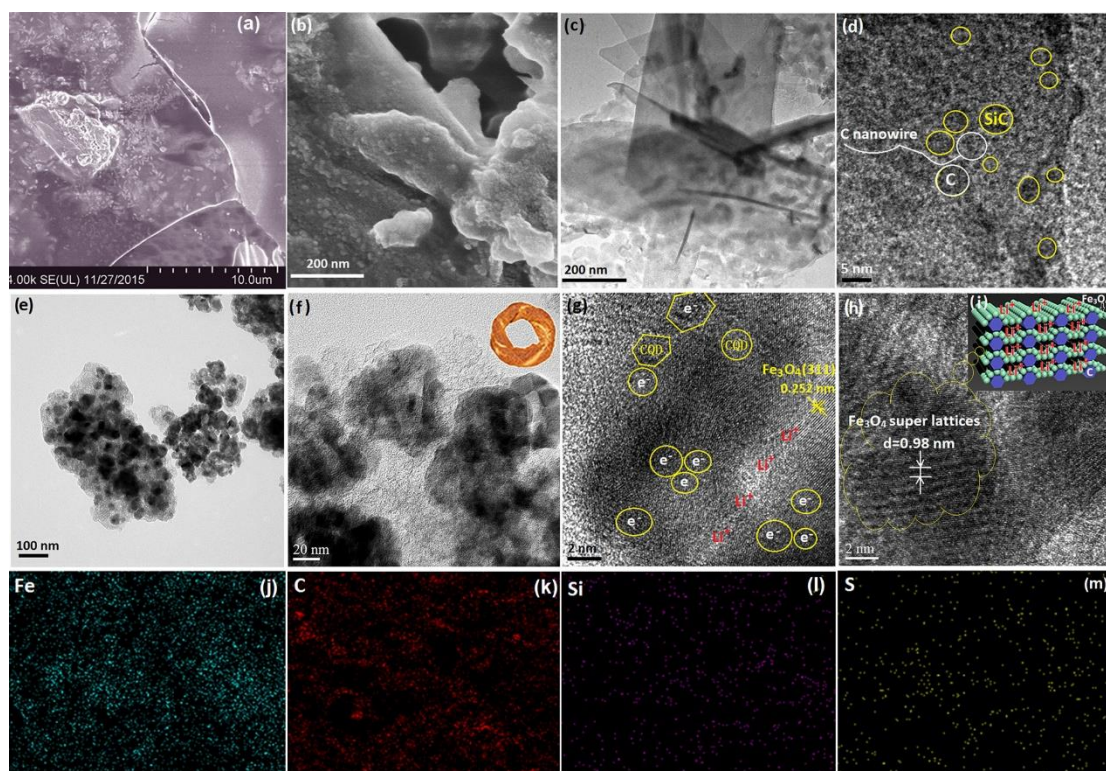
Fig. 2 Microstructure characterizations of the different samples. (ab) SEM images of the dry mixture of SPBL. (c) TEM and (d) HRTEM images of the SPBL ash sample synthesized by carbon thermal reduction reactions at 700 °C. (e) TEM and (f-h) HRTEM images of GCS/FO-NC-D sample. (i) Schematic illustration of the formation of the Fe_3O_4 super lattice structure by using lignins as nanostructral templates and proposed lithium storage by intercalation into the super lattice structure. (j-m) The elemental mapping images of GCS/FO-NC-D sample: iron (j), carbon (k), silicon (l) and sulfur (m).
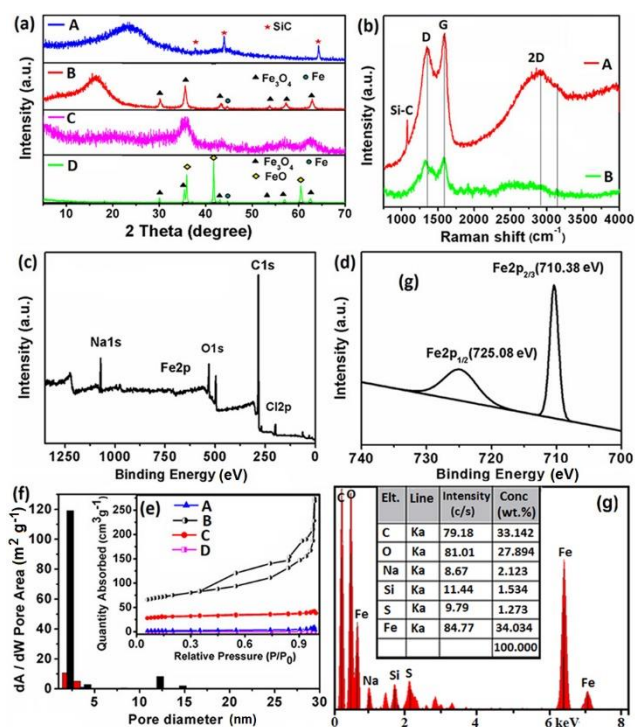
Fig. 3 (a) XRD patterns of the different samples, (A) the SPBL ash sample after the calcination, (B) the lamellar GCS/FO-NC-D sample after the calcination, (C) the GCS/FO-NC-D precursor after the hydrothermal treatment, (D) Fe_3O_4/FeO/Fe blank sample after the calcination. (b) Raman spectra of the SPBL ash (A) and the lamellar GCS/FO-NC-D (B) samples. (c) Survey XPS spectrum and (d) Fe2p spectrum of the lamellar GCS/FO-NC-D sample. (e) N_2 adsorption/desorption isotherms and (f) pore size distribution of the different samples. (g) The energy spectra of GCS/FO-NC-D sample.
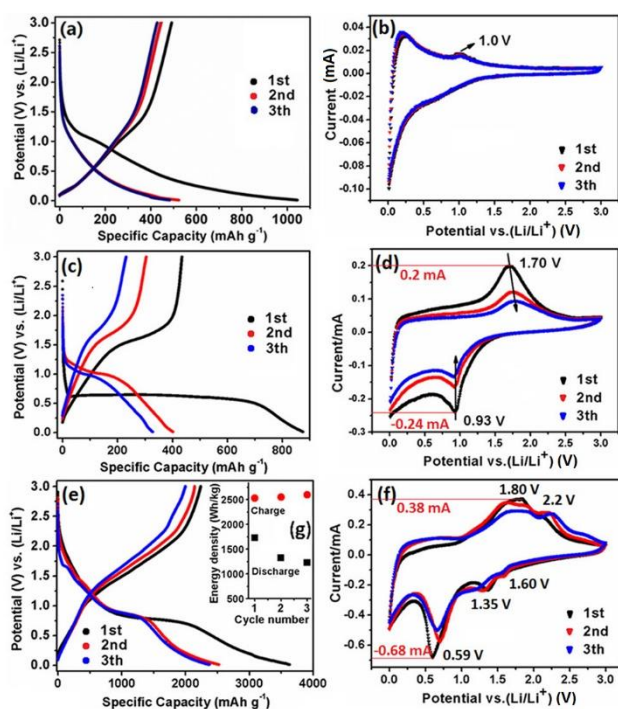
Fig. 4 Electrochemical characterizations. Charge/discharge profiles of the SPBL ash electrode (a), $Fe_3O_4/FeO/Fe$ blank electrode (c) and GCS/FO-NC-D electrode (e) over the first three cycles at 50 mA g^{-1} for LIBs; CV profiles of the SPBL ash (b), $Fe_3O_4/FeO/Fe$ (d) and GCS/FO-NC-D (e) at 0.1 mV s^{-1} scan rate for LIBs; (g) corresponding energy density plot of GCS/FO-NC-D.
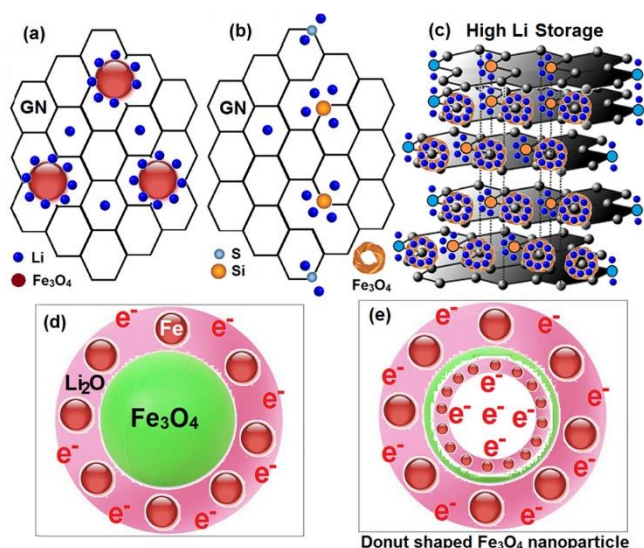
Fig. 5 Schematic representation of the synergy effect between different electrochemical reactions in the GCS/FO-NC electrode. (a) Low Li storage at the atomic interface and an outer surface of traditional Fe_3O_4/CN composite. (b) Low Li storage at the atomic interface of GCS. (c) High Li storage in the interlayer of GCS/FO-NC having a high inner surface area. (de) Schematic of the phase reactions of Fe_3O_4 spheroidal particle (d) and donut shaped Fe_3O_4 nanoparticle with their inner surface (e) during lithiation, exhibiting the different pathway of electron transport at the particle surface.
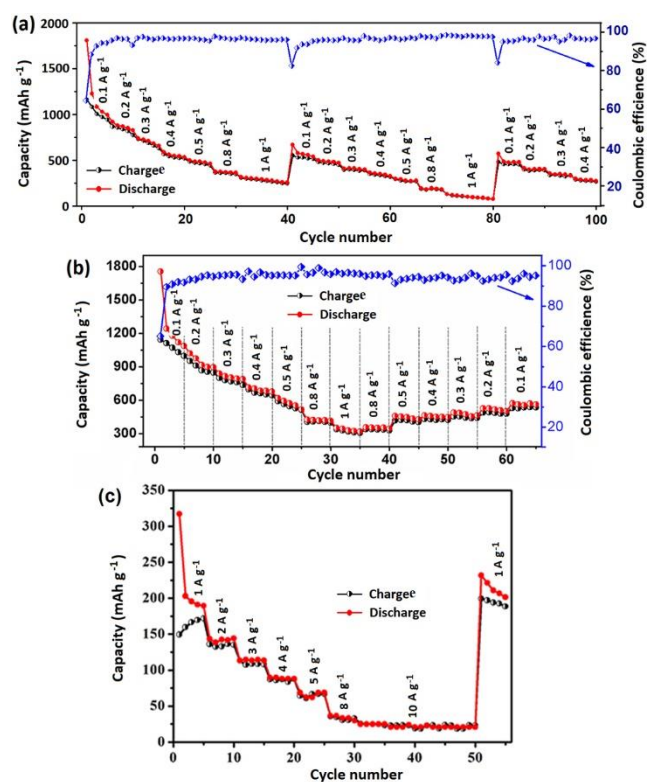
Fig. 6 (a) Rate capability and Coulombic efficiency of GCS/FO-NC-D electrode. (b) Rate capability and Coulombic efficiency of the GCS/FO-NC-D sample synthesized by repeated tests (b) at various current density. (c) High rate capability of the GCS/FO-NC-D sample synthesized by repeated testsfrom 1A g^{-1} to 10A g^{-1}.
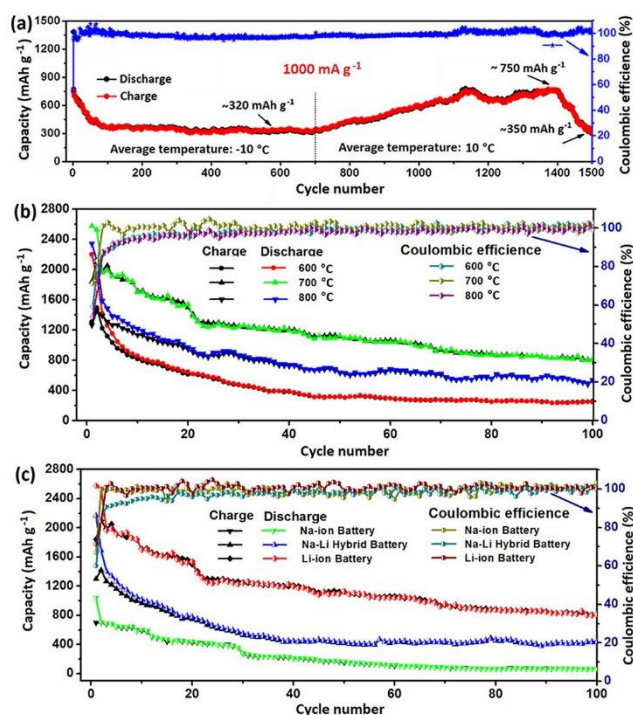
Fig. 7 (a) Cycling stability of the GCS/FO-NC-D electrode at a high current density of 1000 mA g^{-1} for LIBs. (b) Cycle performance comparsion of the nanocomposite electrodes synthesized at different annealing temperature at a current density of 50 mA g^{-1} for 100 cycles in the potential range 0.01-3.0 V for LIBs. (c) Cycling performance comparsion of the GCS/FO-NC-D electrode at the current density of 50 mA g^{-1} for different batteries. Li-ion batteries (LIBs): Li$^+$ electrolyte (1 M LiPF$_6$/EC/DEC/EMC) only and Li metal as a cathode. Na-ion batteries (NIBs) : Na$^+$ electrolyte (1MNaClO$_4$/PC) only and Na metal as a cathode. Na-Li hybrid batteries (NLHBs): Li$^+$/Na$^+$ mixed electrolyte (LiPF$_6$/EC/DEC/EMC and NaClO$_4$/PC in a volume ratio of 1 : 1) and Li metala cathode.